Available online at www.sciencedirect.com
ScienceDirect
Trans. Nonferrous Met. Soc. China 35(2025) 2164−2182
Transactions of Nonferrous Metals Society of China
www.tnmsc.cn

Effects of Al−5Sr−5Sb modifiers prepared by various processes on microstructure, thermal conductivity, and mechanical properties of AlSi10MnMg alloy

Wen-jing LIU[1], Yuan-dong LI[1,2], Zi-chen WANG[1], Xiao-mei LUO[1], Hong-wei ZHOU[1,2], Guang-li BI[1,2]

1. State Key Laboratory of Advanced Processing and Recycling of Nonferrous Metals, Lanzhou University of Technology, Lanzhou 730050, China;
2. Key Laboratory of Nonferrous Metal Alloys and Processing, Ministry of Education, Lanzhou University of Technology, Lanzhou 730050, China

Received 13 December 2023; accepted 7 August 2024

Abstract: Three kinds of Al−5Sr−5Sb modifiers were prepared by permanent mold casting (PMC), controlled diffusion solidification (CDS), and rolling. The influence of the preparation method on Al−5Sr−5Sb was examined by assessing the melting enthalpy from DSC curves and conducting first-principles calculations. Al−5Sr−5Sb was incorporated into AlSi10MnMg alloy to examine the modification effect and mechanism. It is found that the AlSi10MnMg alloy modified with CDS-prepared Al−5Sr−5Sb shows significant improvement in its microstructure, changing the eutectic Si phase from lamellar to coral-like or fiber-like structures. This modification leads to enhanced macroscopic properties: the thermal conductivity is increased by 24.14% to 189.63 W/(m·K), elongation is increased by 59.15% to 10.87%, and tensile strength is increased by 66.9% to 254.98 MPa compared to the unmodified alloy.

Key words: controlled diffusion solidification; modification; AlSi10MnMg; first-principles; thermal conductivity; mechanical properties

1 Introduction

Al−Si alloys, extensively used in the petrochemical, medical, aviation, construction, and military fields, are renowned for their superior casting performance, high specific strength, and low cost [1,2]. The application of Al−Si alloys in electric vehicles has garnered renewed interest, especially with the introduction of concepts such as “integration of automotive structural parts” and “lightweight electric vehicles” [3,4]. Common Al−Si alloys such as A356 and ADC12, known for their excellent mechanical properties and casting performance, are limited by their thermal conductivity, which ranges 120−140 W/(m·K) at room temperature [5,6].

AlSi10MnMg, a hypoeutectic Al−Si alloy, is widely used in electric vehicle production due to its narrow solidification temperature range, high latent solidification heat, and low linear shrinkage coefficient [7]. However, the typically disordered eutectic Si phases, characterized by thick needles, serve as stress points under load, resulting in cracks and adversely impacting the mechanical properties of the alloy [8,9]. Moreover, the Si phase in Al−Si alloys significantly obstructs free electron transfer, impacting the thermal conductivity of alloy [10].

Modifying the alloy by adding single or multiple elements to refine the α(Al) and Si phases is an established method for preparing Al−Si alloys [11]. Common aluminum modifiers include

Corresponding author: Yuan-dong LI, Tel: +86-931-2976795, E-mail: liyd_lut@163.com
https://doi.org/10.1016/S1003-6326(25)66807-5

B, Sr, Na, P, Ti, and RE, with combinations such as Sr+ RE, Ti+ B, Na+ Sr, and P+B used in composite modifications [12,13]. Composite modification generally surpasses single-modification treatment in Al−Si alloys. Nevertheless, composite modification treatment typically involves incorporating multiple modifying elements into the alloy, along with complex temperature control during the process, which can result in issues such as increased preparation costs. Composite modifiers, however, effectively mitigate these challenges [14].

Sr can effectively transform eutectic Si from a thick needle-like structure to a fiber-like structure and enhance the mechanical properties of the alloy. However, Sr tends to increase the inspiratory tendency of the melt, leading to defects such as shrinkage porosity [15]. Moreover, some studies have indicated that adding Sr can improve the thermal conductivity of hypoeutectic Al−Si alloys, with the refinement of eutectic Si being the primary contributing factor [16,17]. Additionally, introducing an appropriate amount of Sb to the alloy melt can reduce its inspiratory tendency, increase its densification, and enhance its mechanical properties [18]. However, Sb addition has minimal impact on the thermal conductivity of aluminum [19]. Consequently, Sr and Sb were used to prepare the modifier, each compensating for the limitations of the other, thereby achieving a more effective modification.

The most commonly employed methods for preparing modifiers include infiltration, thermal reduction, and fused salt electrolysis [20,21]. These methods necessitate complex equipment and stringent process control for composite modifier preparation.

Permanent mold casting (PMC) produces castings characterized by a high surface finish, simple processing, and rapid cooling, making it suitable for modifier preparation. Controlled diffusion solidification (CDS) involves mixing two alloy melts (parent alloys) of different compositions and temperatures to obtain a target alloy melt slightly below the liquidus temperature [22,23]. CDS offer a fine, uniform product structure, high melt purity, and minimal equipment investment, making it suitable for preparing composite modifiers [24]. Rolling, which is crucial for refining grain size and improving alloy microstructure [25], effectively enhances the modifying effect of the Al−Sr−Sb modifier through microstructure and phase improvement.

Considering the inverse relationship between thermal conductivity and mechanical properties in aluminum alloys, it is crucial to develop a composite modifier through various preparation processes. This approach aims to enhance the thermal conductivity and mechanical properties of Al−Si alloys while minimizing costs associated with alloying structural defects and preparation procedures.

2 Experimental

The Al−Sr−Sb modifier was prepared using Al−10Sr and Al−10Sb master alloys, and the Al−5Sr−5Sb modifier was produced through permanent mold casting (PMC), controlled diffusion solidification (CDS), and rolling.

Based on previous research [26], 4 wt.% Al−5Sr−5Sb modifier was added to commercial AlSi10MnMg alloys to assess the effectiveness of the modification using the PMC process. The chemical composition of the alloy was analyzed using ICP−AES, as detailed in Table 1.

Table 1 Chemical composition of experimental alloys (wt.%)

Alloy	Si	Mn	Mg	Ti	Fe	Sr	Sb	Al
AlSi10MnMg	10.41	0.58	0.337	0.14	0.076			Bal.
Al−10Sr						10.46		Bal.
Al−10Sb							9.87	Bal.
Al−5Sr−5Sb (PMC)						4.88	5.43	Bal.
Al−5Sr−5Sb (CDS)						4.79	5.19	Bal.
Al−5Sr−5Sb (rolled)						4.92	5.32	Bal.

2.1 Material preparation

2.1.1 Al−5Sr−5Sb preparation by PMC

During the PMC process, the Al−10Sr and Al−10Sb master alloys were first placed in a resistance furnace and melted at 790 °C. Once fully melted, the mixture was stirred with a graphite rod, and 1 wt.% covering agent (0.5 wt.% NaCl + 0.5 wt.% KCl) was evenly distributed over the surface of the melt. The temperature of the melt was then adjusted to 760 °C and held steady for 30 min. After insulation, the melt was poured into a preheated metal-type mold at 250 °C to obtain an alloy test bar of *d*18 mm×150 mm.

2.1.2 Al−5Sr−5Sb preparation by CDS

As illustrated in Fig. 1(a), the CDS process involves two SRJX-4−12 resistance furnaces to melt the Al−10Sr and Al−10Sb master alloys. Furnace No. 1 was heated to 720 °C, and Furnace No. 2 was heated to 820 °C. Al−10Sb low-temperature melt was prepared in Furnace No. 1. In contrast, Al−10Sr high-temperature melt was prepared in Furnace No. 2. After the master alloys were melted and maintained warm for 15−20 min, the high-temperature melt from Furnace No. 1 was quickly poured into Furnace No. 2 and stirred. Once the mixed melt temperature reached 740−750 °C, it was cast into a preheated 250 °C permanent mold to form samples of the same size as those prepared by PMC.

2.1.3 Al−5Sr−5Sb preparation by rolling

Figure 1(b) shows a schematic of the rolling process. A cut steel plate was polished, cleaned, and brushed with a release agent during this process. The Al−10Sr and Al−10Sb master alloys were melted in a resistance furnace, reaching and maintaining a temperature of 770 °C for 30 min. Once the insulation was complete, the roll gap was set to be 7 mm, and the roll speed was set to be 50 r/min. The rolling mill was initiated at room temperature, and the alloy melt was poured onto the prepared steel plate and passed through the rolls for rolling, followed by air cooling. The alloy specimen was then removed from the steel plate.

2.1.4 Modification of AlSi10MnMg

Three Al−5Sr−5Sb modifiers were added to the AlSi10MnMg alloy by PMC, each constituting 4 wt.% of the alloy. During the melting, the AlSi10MnMg alloy was first placed in a graphite crucible inside a resistance furnace and heated to 730 °C to melt the alloy. The Al−5Sr−5Sb modifier was introduced into the AlSi10MnMg melt upon reaching 740 °C. Once the modifier was completely dissolved, it was uniformly dispersed using a graphite rod and held for 30 min. Following this, the melt temperature was adjusted to 720 °C, and C_2Cl_6 was introduced for refining and slag removal. Following refining, the melt temperature was adjusted to 690 °C, and the sample was poured into a preheated 250 °C metal mold to cast an alloy test bar with dimensions of *d*18 mm×150 mm.

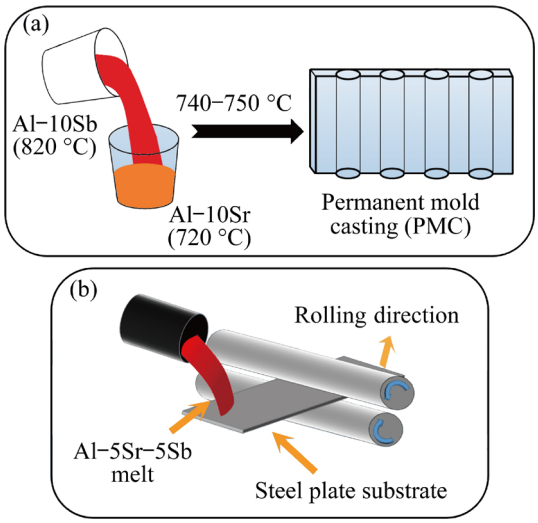

Fig. 1 Schematic of preparation of Al−5Sr−5Sb: (a) CDS; (b) Rolling

2.2 Material characterization and property testing

The Archimedes drainage method was utilized to measure the density of the alloy samples. An LFA457 laser thermal conductivity instrument was used to assess the thermal diffusivity of the samples, and an STA449C simultaneous thermal analyzer was used to measure the specific heat capacity and DSC curves. Three specimens for each experimental parameter were selected, with the average value considered as the final result. The thermal conductivity (λ) is calculated using the following formula:

$$\lambda=\rho\alpha c_p \quad (1)$$

where ρ is the density (g/cm^3), α is the thermal diffusion coefficient (mm^2/s), and c_p is the specific heat capacity (J/g·K).

The DK7−725 EDM CNC cutting machine was used to sample the center of the alloy test bar (*d*12.7 mm × 3 mm) for microstructure observation and thermal conductivity testing. The mechanical

properties were tested on a WDW−100D electronic universal material testing machine with a tensile rate of 0.5 mm/min and a measurement length of 20 mm. The dimensions of the tensile specimen are shown in Fig. 2; three specimens for each experimental parameter were selected, and the average value was calculated as the result.

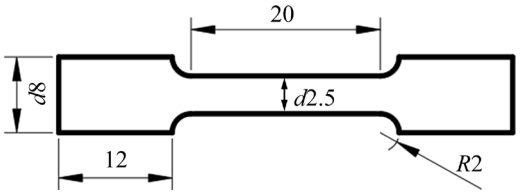

Fig. 2 Dimensions of tensile specimen (Unit: mm)

2.3 Microstructure characterization

The specimens for microstructure analysis were extracted from the central region of the cross-section of the cast aluminum alloy bar. X-ray diffraction (XRD, D8−ADVANCE) was employed to analyze the alloy phases under the following test conditions: an operating voltage and current of 40 kV and 40 mA, respectively, a scanning speed of 2 (°)/min, and a scanning angle range from 20° to 90°. Optical microscopy (OM, Axio Scope A1) was utilized to examine the grain distribution and size within the alloys. Scanning electron microscopy (SEM, QUANTA FEG−450) was used to examine the morphology and distribution of some second phases, such as intermetallics and primary precipitates. Energy dispersive spectroscopy (EDS) was used to analyze the concentration of alloying elements and intermetallic compounds in the microzone as well as the phase composition. The OM and SEM specimens were ground and polished using a series of SiC grinding papers (400−2000 grit) followed by a diamond polishing agent (5 μm). The OM and SEM testing specimens were also etched after polishing with Keller's reagent (95 mL water, 2.5 mL HNO_3, 1.5 mL HCl, and 1 mL HF).

2.4 Computational details

First-principles calculations were performed using the Cambridge Sequential Total Energy Package (CASTEP) code, based on density functional theory (DFT) [27]. The Kohn–Sham equations were solved using the plane-wave pseudopotential technique [28], with the exchange−correlation function in the electron–electron interaction treated using the Perdew–Burke–Ernzerhof (PBE) function [29] and the generalized gradient approximation (GGA) [30,31]. The crystal structure was geometrically optimized using the Broyden−Fletcher−Goldfarb−Shanno (BFGS) method [32]. Various cutoff energies were tested: 550 eV for the Al−5Sr−5Sb calculations and 440 eV for the Al_4Sr, AlSb, and Sr_2Sb calculations. The 7×7×7 and 6×6×6 *k*-point meshes produced an irreducible Brillouin zone in cubic Al−5Sr−5Sb and AlSb, while a 10×10×4 (7×7×2) *k*-point mesh was used for the tetragonal Al_4Sr (Sr_2Sb) phases. The Hellman–Feynman force per atom was minimized to less than 0.01 eV/Å. The calculated equilibrium unit cell volume is used to determine other properties.

3 Results and discussion

3.1 Microstructures of Al−5Sr−5Sb modifier prepared by different methods

The microstructures of the Al−5Sr−5Sb modifiers prepared by different processes are shown in Fig. 3. Compared to PMC (Fig. 3(a)), CDS (Fig. 3(b)) and rolling (Fig. 3(c)) more effectively refine the α(Al) grains (Fig. 4). In the CDS process, the rapid mixing of high-temperature and low-temperature melts near liquid conditions results in supercooling and temperature variance in certain regions. Mixing melts with different solute concentrations results in atomic clusters in the mixed melt, leading to temperature and concentration fluctuations in the alloy melt, providing two primary conditions for nucleation. Hence, numerous critical nuclei is formed in the mixed melt instantly, refining the grains [33,34]. During the rolling process, plastic deformation during rolling refines the grains [35]. Consequently, the microstructure of the Al−5Sr−5Sb modifier prepared from CDS is more pronouncedly refined than that of PMC.

The XRD patterns of Al−5Sr−5Sb prepared through various methods are illustrated in Fig. 5. The analysis reveals consistent phases in the Al−5Sr−5Sb modifier, primarily Al, Al_4Sr, AlSb, and Sr_2Sb, regardless of the preparation method employed. The presence of Al_4Sr and AlSb is critical to the efficacy of the Al−5Sr−5Sb modifier, with Al_4Sr aiding in the diffusion of Sr atoms within the Al−Si alloy melt. However, the impact of this change becomes evident only when the Sr

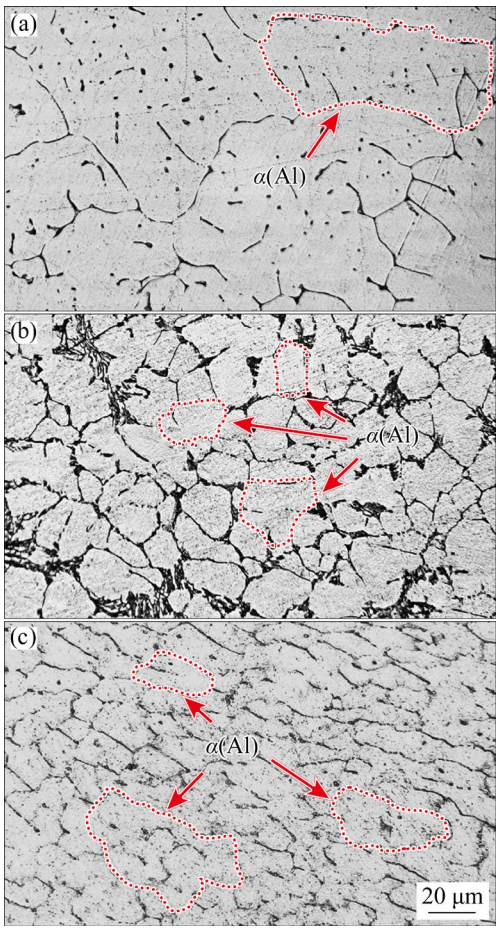

Fig. 3 Microstructures of Al−5Sr−5Sb modifiers with different preparation processes: (a) PMC; (b) CDS; (c) Rolling

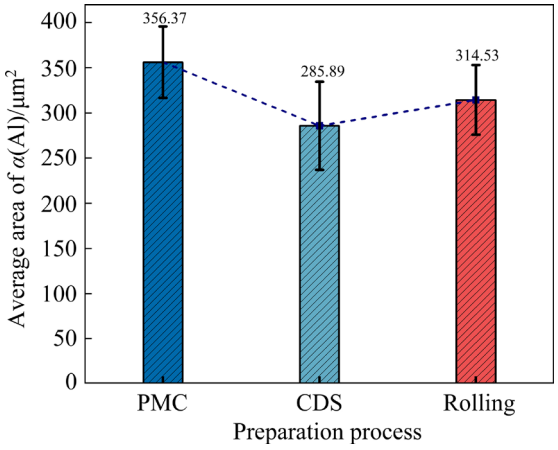

Fig. 4 Average area of α(Al) of Al−5Sr−5Sb modifiers with different preparation processes

atoms reach adsorption equilibrium with the crystal embryos of Si phase [36]. Thus, the effectiveness of the modifier is contingent upon the capacity of Al_4Sr to dissociate Sr atoms, with the extent of dissociation influenced by the morphology and size of Al_4Sr [37]. In AlSb, the presence of Sb alters the liquid phase structure, promoting Si atom clustering and forming the eutectic Si phase, thereby enhancing its stability. However, it does not transform the morphology of the eutectic Si phase into a fiber-like structure [38].

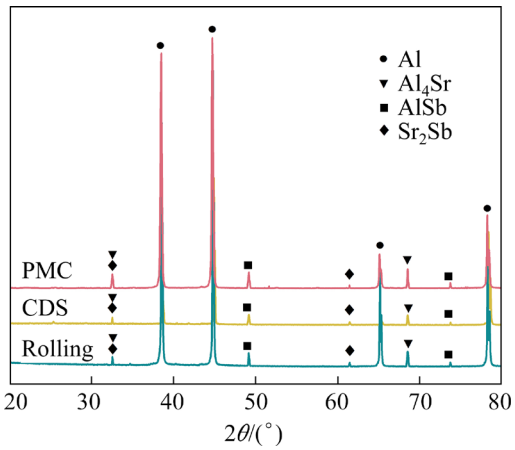

Fig. 5 XRD patterns of Al−5Sr−5Sb modifiers prepared by different processes

The SEM images (Fig. 6) reveal that the preparation method significantly affects the morphology and size of the precipitates in the alloy. The EDS point scanning results (Fig. 7), combined with the Al−Sr and Al−Sb phase diagrams and the XRD pattern (Fig. 5), confirm that the main precipitated phases in the Al−5Sr−5Sb modifier are Al_4Sr and AlSb. In PMC-prepared Al−5Sr−5Sb (Fig. 6(a)), Al_4Sr is distributed in α(Al) in long strip shapes, and AlSb aggregates around grain boundaries in irregular granular or spherical shapes. In the CDS-prepared modifier (Fig. 6(b)), Al_4Sr is significantly refined, transforming from strip to finer, smaller fiber-like shapes; AlSb appears as long needle-like and irregular block-like structures, with some clustering at grain boundaries. The rolling process (Fig. 6(c)) results in smaller Al_4Sr than PMC, maintaining a strip-like shape and a prevalence of granular AlSb compared to the needle-like structures in the CDS-prepared alloy.

In general, the size and morphology of Al_4Sr and AlSb significantly affect the modification performance, which is also affected by the preparation process. For example, according to industrial practices, the modification efficiency depends upon the dissolution and diffusion rates of the phases, which are related to their morphology, size, and defects [39].

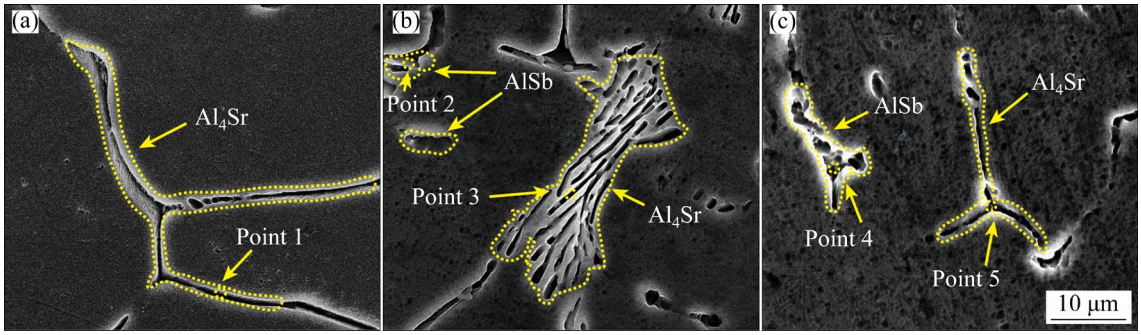

Fig. 6 SEM images of Al−5Sr−5Sb modifiers after different preparation processes: (a) PMC; (b) CDS; (c) Rolling

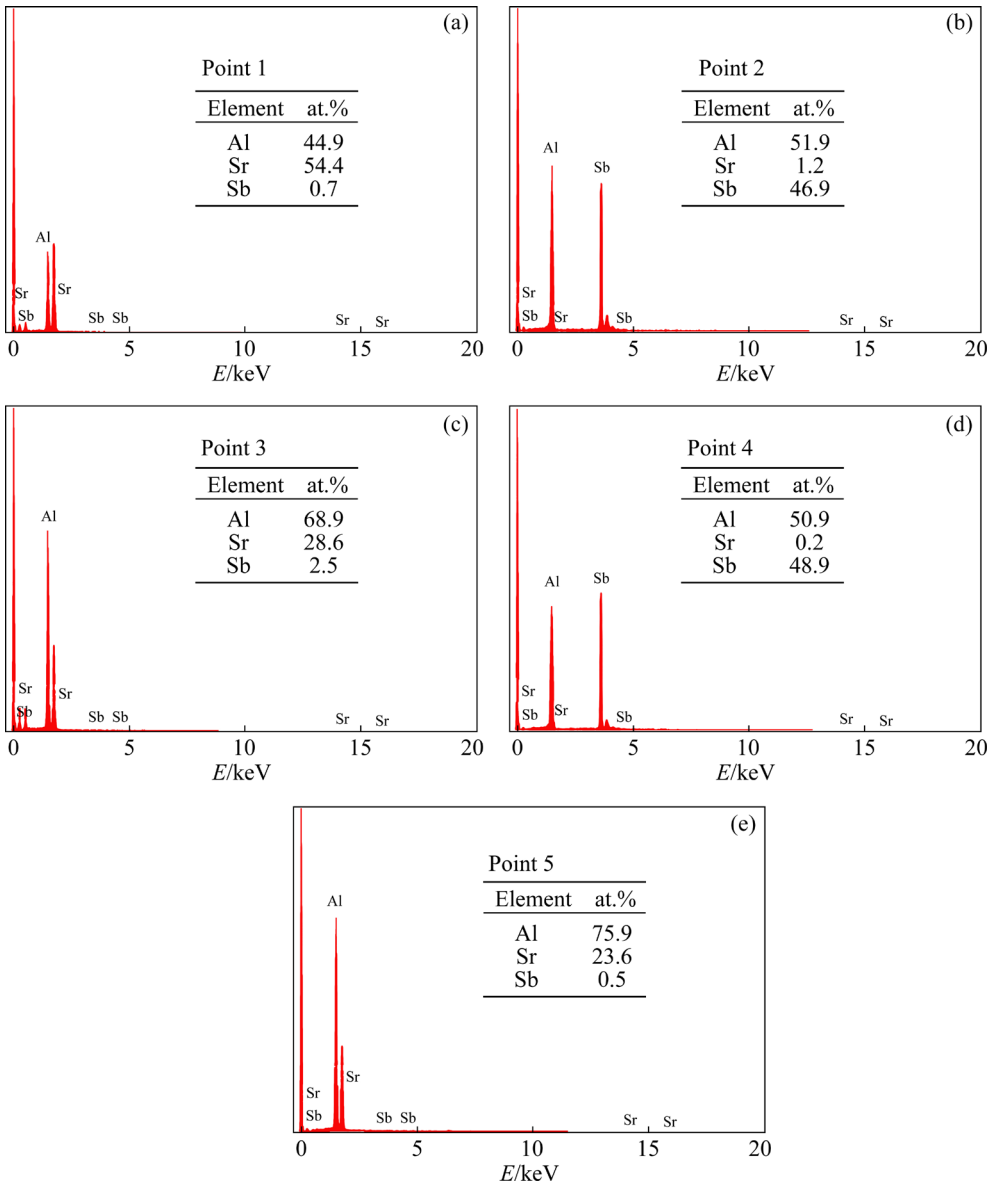

Fig. 7 EDS point scanning results of Al−5Sr−5Sb in Fig. 6: (a) Point 1; (b) Point 2; (c) Point 3; (d) Point 4; (e) Point 5

Image-Pro Plus 6.0 software was used to measure the lengths of Al_4Sr and AlSb in 10 SEM images from different experiments, and the results are presented in Fig. 8.

The average sizes of Al_4Sr and AlSb in Al−5Sr−5Sb, which were prepared through CDS and rolling, are smaller than those in the modifier prepared via PMC. Specifically, the average size of

Al_4Sr prepared through CDS is 107.89 μm, while that of AlSb is 52.43 μm. Therefore, CDS is proven to be a more suitable method for preparing the Al−5Sr−5Sb modifier.

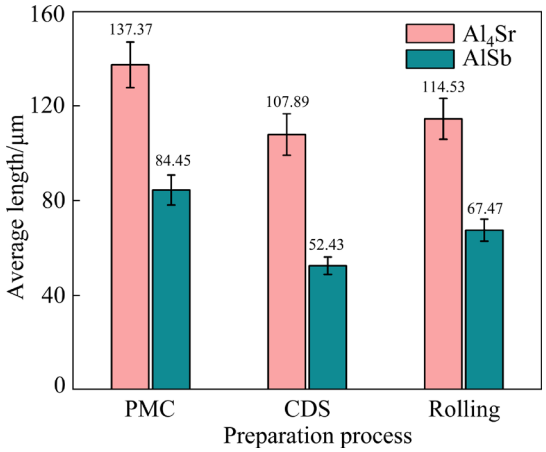

Fig. 8 Average length of Al_4Sr and AlSb in Al−5Sr−5Sb with different preparation processes

In Fig. 9(a), the DSC curves illustrate the behavior of the Al−5Sr−5Sb modifier with different preparation processes at a heating rate of 20 K/min. To determine the melting enthalpy of the Al−5Sr−5Sb modifier, the heat absorption peaks in the DSC patterns were integrated over time for three preparation processes. The results are depicted in Fig. 9(b). Notably, the Al−5Sr−5Sb modifier prepared through PMC exhibits the highest melting enthalpy, reaching 410.6 J/g. In contrast, the Al−5Sr−5Sb alloy achieves a melting enthalpy of 356.1 J/g after rolling, while the Al−5Sr−5Sb alloy prepared via CDS has the lowest melting enthalpy of 308.9 J/g.

The variations in alloy structure reflect the differences in the melting enthalpy of the Al−5Sr−5Sb alloy with different preparation processes. Notably, intergranular structures, such as Al_4Sr, produced through CDS exhibit finer characteristics than the modifiers prepared via PMC and rolling. This finer structure increases the surface free energy of Al_4Sr and AlSb, thereby elevating the energy of the alloy system and resulting in the lowest melting enthalpy.

When Al−5Sr−5Sb modifiers are introduced into the Al−Si alloy melt through various processes, the one with the lowest melting enthalpy, as seen with Al−5Sr−5Sb prepared through CDS, generates the most energy within the entire melt [40]. This phenomenon accelerates the decomposition of the Al_4Sr and AlSb phases into Sr and Sb atoms, which subsequently diffuse extensively throughout the eutectic Si, influencing its growth pattern. Moreover, Sb contributes to more thorough refinement of the eutectic Si phase.

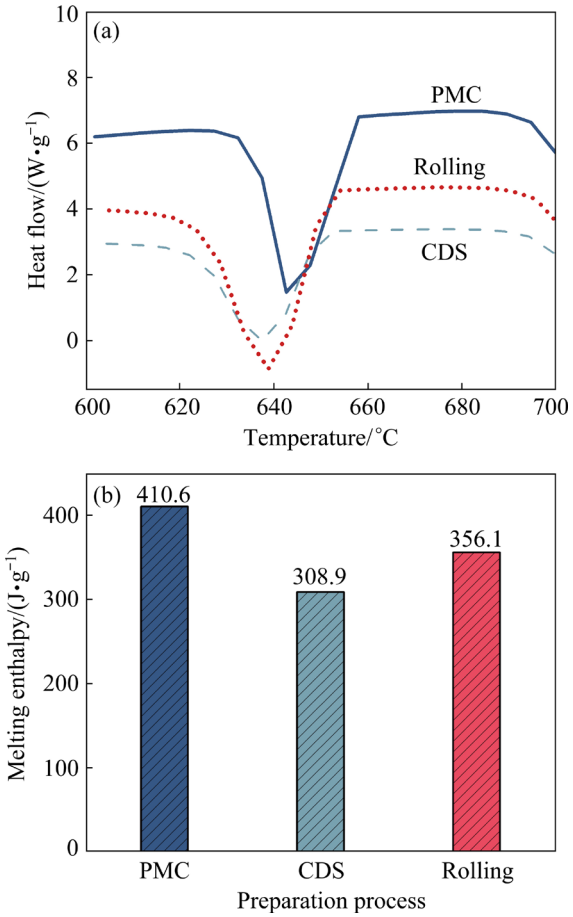

Fig. 9 DSC curves and melting enthalpy of Al−5Sr−5Sb prepared by different processes: (a) DSC curves; (b) Melting enthalpy

In the EDS point scan of the Al−5Sr−5Sb modifier, a minimal presence of a round particle phase is observed, as depicted in Fig. 10. Analysis of the EDS point scanning results, XRD patterns (Fig. 5), and the Sr−Sb phase diagram identifies this circular particle phase as Sr_2Sb. IVANOV et al [41] determined the mixing enthalpy of a Sr−Sb melt using isoperibolic calorimetry, revealing a melting enthalpy, ΔH_{min}, of (−70.1±4.8) kJ/mol. This indicates a significant exothermic mixing effect in the Sr−Sb system, suggesting a strong interaction between the Sr−Sb components, in alignment with the Sr−Sb phase diagram.

3.2 First-principles study

A 2×2×2 FCC supercell model containing 32

Al atoms was constructed. To replicate the chemical composition, 6 Sr atoms and 4 Sb atoms replaced 10 Al atoms, forming an Al−5Sr−5Sb ($Al_{22}Sr_6Sb_4$) alloy supercell model, as shown in Fig. 11(a). The Debye temperature of Al−5Sr−5Sb, ranging from 0 to 1400 K, is presented in Fig. 11(b). This temperature increases between 0 and 1400 K, following the T^3 law of the Debye model. The Debye temperature at room temperature, 367.8 K, suggests weak interatomic forces within the material.

The electronic properties of Al−5Sr−5Sb were deduced from the electronic band structure, along with the total and partial density of states. These findings provide insights into the conductivity and bonding characteristics of the materials. The band structure, observed in Fig. 11(c), shows an overlap of the valence and conduction bands at the Fermi level, indicating metallic characteristics with E_f=0. The predominance of Al S-electrons in Al−5Sr−5Sb is evident, as shown in Fig. 11(d).

The Fermi level, indicated by a dotted line, intersects the aluminum s-like and p-like states, Sr s-like states, and Sb s-like and p-like states, demonstrating the conducting nature of the material. The calculated total density of states for

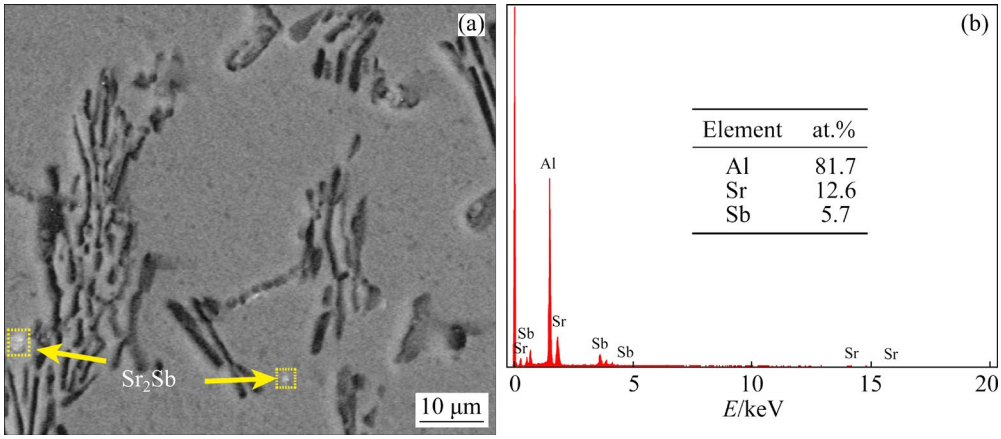

Fig. 10 EDS point scanning results of Sr_2Sb: (a) SEM image of Sr_2Sb; (b) Point scanning spectrum of Sr_2Sb

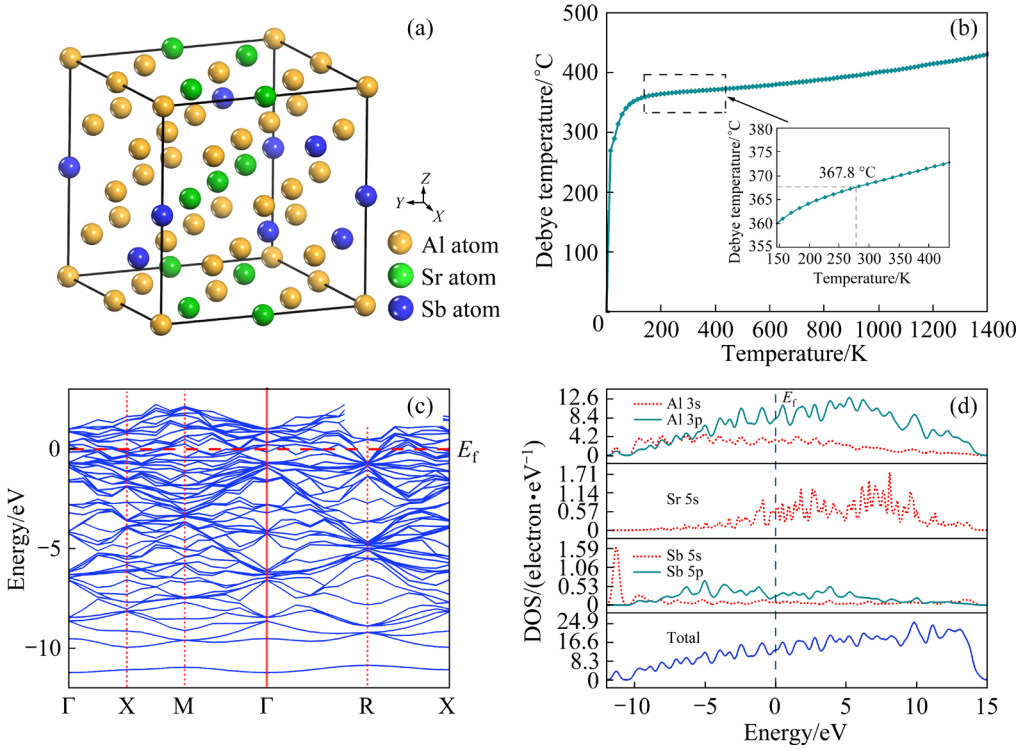

Fig. 11 Calculations results of Al−Sr−Sb: (a) Al−5Sr−5Sb structure ($Al_{22}Sr_6Sb_4$); (b) Debye temperature of Al−Sr−Sb; (c) Electronic band structure of Al−Sr−Sb; (d) Total and partial density of states of Al−Sr−Sb

Al−5Sr−5Sb reveals a significant contribution from the s-electrons of Al, which is crucial to determining the conductivity and bonding properties of the alloy.

Conventional experimental methods are efficient at evaluating the specific phase performance of alloys. To understand the effect of the AlSb, Al_4Sr, and Sr_2Sb phases on the Al−5Sr−5Sb properties (Fig. 12), XRD patterns (Fig. 5) were analyzed. Table 2 lists the crystal structures and lattice constants of each phase derived from these calculations.

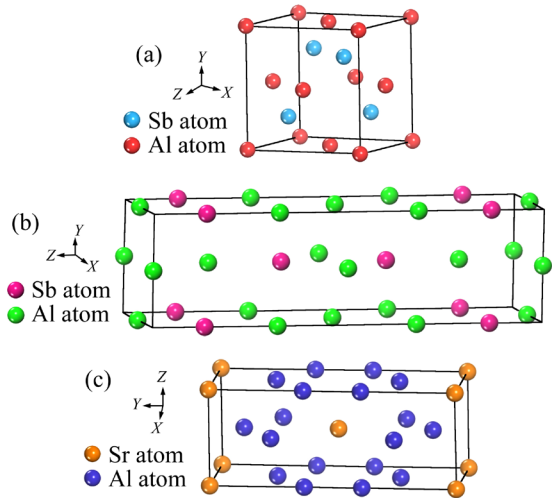

Fig. 12 Optimized geometry models: (a) AlSb; (b) Sr_2Sb; (c) Al_4Sr

Table 2 Lattice structure and lattice constants of Al_4Sr, AlSb, and Sr_2Sb

Phase	Space group	Crystal system	Lattice constant		
			a/Å	b/Å	c/Å
Al_4Sr	$I4/mmm$	Tetragonal	4.44	4.44	11.21
AlSb	$F\overline{4}3m$	Cubic	6.19	6.19	6.19
Sr_2Sb	$I4/mmm$	Tetragonal	5.05	5.05	17.83

The Debye temperature (θ_D) is integral for assessing a material's structural stability and bonding strength. A high θ_D typically signifies strong chemical bonds and superior thermal conductivity [42]. The Debye temperature can usually be calculated by the average acoustic velocity (V_m) [43]:

$$\theta_D = V_m \frac{h}{k_B}\left[\frac{3n}{4\pi}\cdot\left(\frac{N_A\rho}{M}\right)\right]^{1/3} \quad (2)$$

where h is Planck's constant, k_B is Boltzmann's constant, N_A is Avogadro's constant, ρ represents the density of the compound, M indicates the molar mass of the compound, and n represents the total number of atoms in each chemical formula. The average bulk modulus (B_H) and average shear modulus (G_H) of the intermetallic compound were determined using CASTEP. The transverse and longitudinal velocities of the material phonons, V_t and V_l, respectively, and the average acoustic wave velocity, V_m, can be approximated by the following equation:

$$V_m = \left[\frac{1}{3}\cdot\left(\frac{1}{V_l^3}+\frac{2}{V_t^3}\right)\right]^{-1/3} \quad (3)$$

$$V_l = \left[\left(B+\frac{4}{3}G\right)/\rho\right]^{1/2} \quad (4)$$

$$V_t = [G/\rho]^{1/2} \quad (5)$$

Table 3 presents the B_H, G_H, and B/G values, Poisson's ratio, and θ_D for each phase. The B/G values, according to Pugh's empirical criterion [44], indicate material ductility. A higher B/G value implies better plastic toughness, while a lower value indicates fragility, with a critical boundary of 1.75. The Poisson's ratio (v) reflects the ductility strength of the material [45]:

$$v = \frac{3B_H - 2G_H}{6B_H + 2G_H} \quad (6)$$

The B/G values of Al_4Sr and Sr_2Sb, which are close to 1.75, suggest their brittle nature. The B/G value of AlSb is 1.36, which is the smallest for Al−5Sr−5Sb and below Pugh's critical value, indicating fragility and resistance to deformation.

Table 3 CASTEP calculation results

Phase	B_H/GPa	G_H/GPa	B/G	v	ρ/cm^{-3}
Al_4Sr	53.21	31.65	1.68	0.264	2.93
AlSb	26.91	19.77	1.36	0.197	4.33
Sr_2Sb	49.74	30.32	1.64	0.255	4.18

The Debye temperature is pivotal for determining the thermophysical properties of the materials. This is associated with the lattice thermal conductivity of a solid, where a higher Debye temperature usually indicates superior thermal conductivity at room temperature [46]. The calculated Debye temperature (θ_D), as presented in Fig. 13, reveals an increase in Debye temperature of

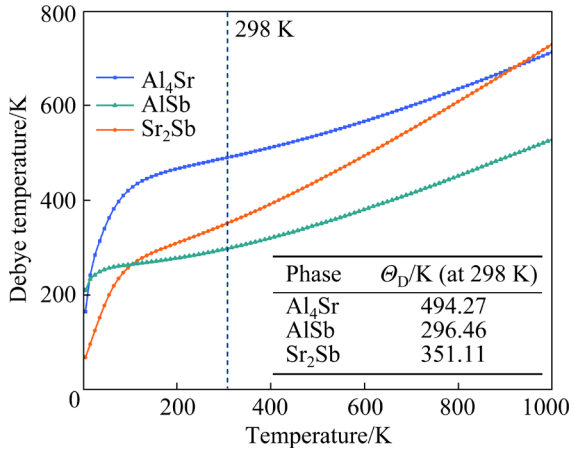

Fig. 13 Debye temperature of phases

the studied compounds with increasing the temperature. In the Al−5Sr−5Sb alloy, the Debye temperatures of the phases, Al_4Sr, Sr_2Sb, and AlSb, are in descending order. The highest Debye temperature at room temperature is observed for Al_4Sr, at 494.27 K, whereas AlSb and Sr_2Sb exhibit lower temperatures of 296.46 K and 351.11 K, respectively. Lower Debye temperature in AlSb adversely affects the thermal conductivity of modified Al−Si alloys [47].

This study examines the electrical properties and bonding characteristics of Al_4Sr, AlSb, and Sr_2Sb. Figure 14 illustrates their electronic band structures and density of states. The energy band

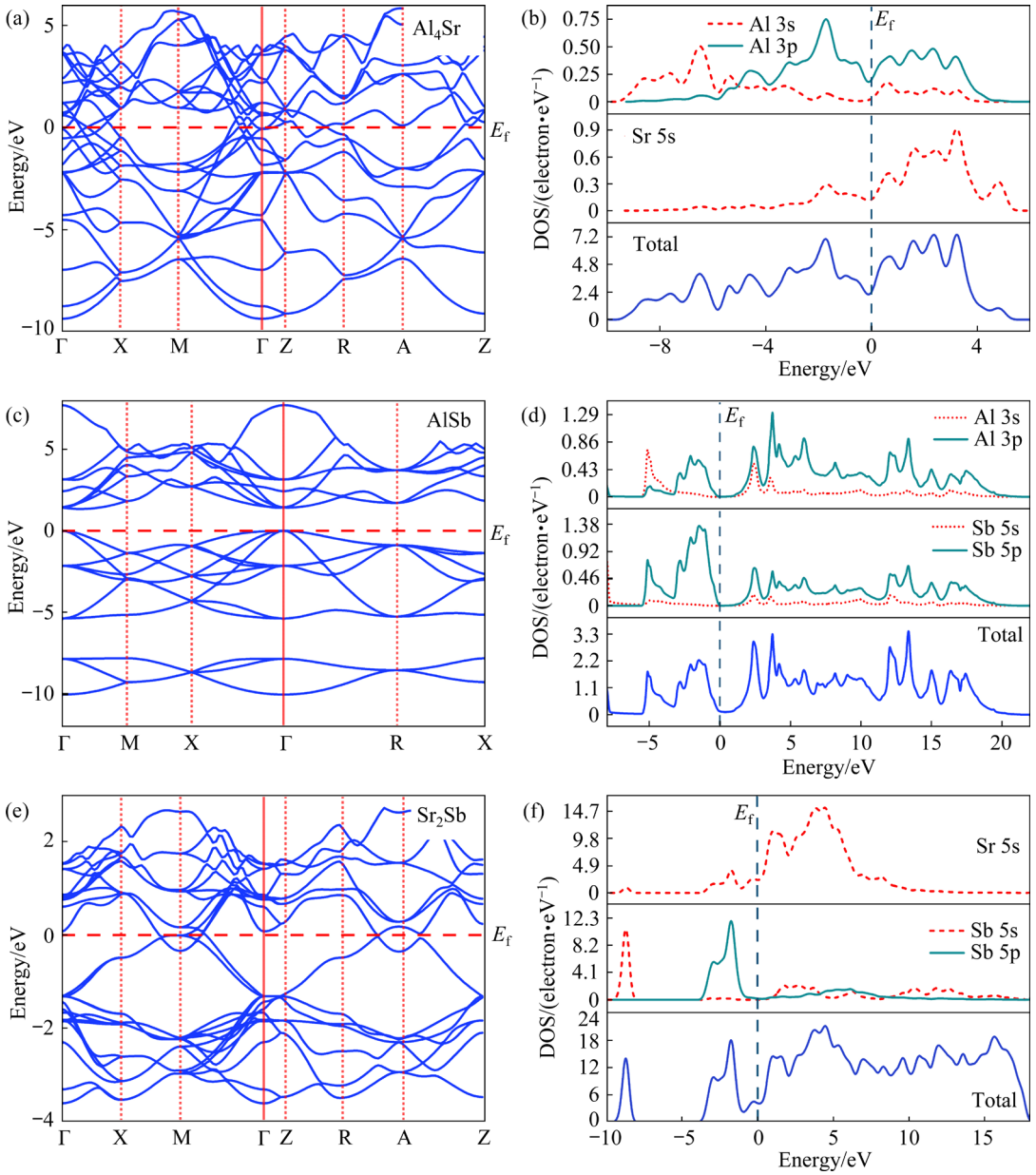

Fig. 14 Electronic band structure (a, c, e) and density of states (b, d, f) of Al_4Sr (a, b), AlSb (c, d), and Sr_2Sb (e, f) phases

profiles in Figs. 14(a, e) indicate an overlap of valence and conduction bands of Al_4Sr and Sr_2Sb at the Fermi energy level, suggesting their metallic properties. Figure 14(c) depicts the energy band structure of AlSb, showing a direct band gap and its semiconductor nature. These band structures correspond to the Debye temperatures (Fig. 13). In Al_4Sr and Sr_2Sb, the dominance of Al s-electrons and Sr s-electrons is evident, as indicated in Figs. 14(b, f). Moreover, the Fermi level in Al_4Sr, indicated by a dotted line, intersects the s-like and p-like states of Al and the s-like state of Sr. In Sr_2Sb, the Fermi level engages with the s-like states of Sr and s-like and p-like states of Sb, reflecting the metallic and conducting characteristics of both compounds. Notably, AlSb displays a DOS value of 0 near the Fermi level, as depicted in Fig. 14(d). This characteristic, in combination with the AlSb energy band structure, reveals a semiconducting nature due to a band gap.

Whether compounds exhibit a ductile or brittle nature can be determined by analyzing the electron density of states at the Fermi level [48]. The computational findings indicate that both the Al_4Sr and Sr_2Sb compounds exhibit a DOS value at the Fermi level, in contrast to AlSb (Fig. 14). Based on these results, it can be confidently concluded that both Al_4Sr and Sr_2Sb possess a brittle nature, which aligns with the results obtained from the B/G ratio, as shown in Table 3.

3.3 Effect of Al−5Sr−5Sb modifier prepared with different methods on AlSi10MnMg alloy

The effectiveness of the PMC-, CDS-, and rolling-prepared Al−5Sr−5Sb modifiers in the AlSi10MnMg alloys was assessed. Figure 15 compares the microstructures of the unmodified and modified AlSi10MnMg alloys. The primary features of the unmodified alloy include α(Al) and eutectic Si, with the former appearing light-colored and the latter appearing dark-colored in the figure. The needle-like, disorderly distributed eutectic Si in the unmodified alloy (Fig. 15(a)) contrasts sharply with that in the modified alloy, where α(Al) is refined, eutectic Si is diffused, and the continuity of the alloy matrix is enhanced.

The size of the α-Al was evaluated through the secondary dendrite arm spacing (SDAS) characterization utilizing Image-Pro Plus 6.0 software (Fig. 16). The SDAS measurements were calculated in a vertical cross section, exhibiting a uniform arrangement consistent with the orientation of dendrites. This arrangement facilitates the attachment of a second dendritic crystal to the same dendrite, with the gap between secondary dendrite arms indicated by λ_2.

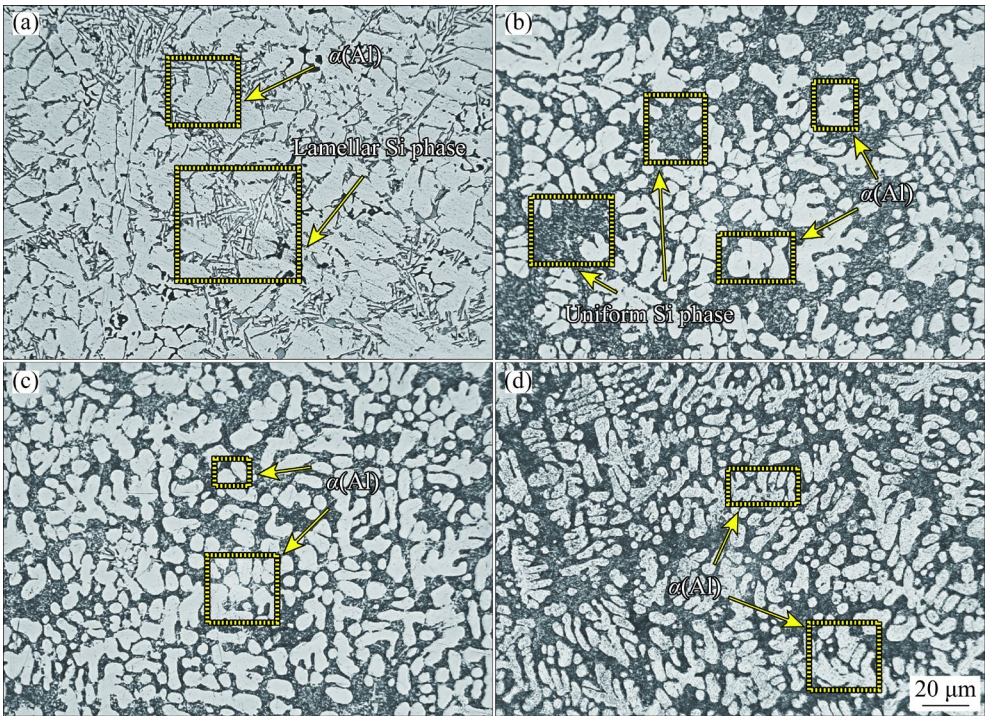

Fig. 15 Microstructures of AlSi10MnMg alloys unmodified (a) and modified with Al−5Sr−5Sb prepared by different processes: (b) PMC; (c) CDS; (d) Rolling

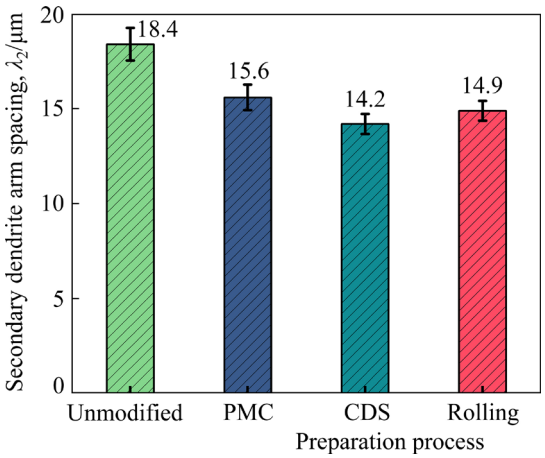

Fig. 16 Secondary dendrite arm spacing (λ_2) of α(Al) phase unmodified and after addition of Al−5Sr−5Sb modifier prepared by different processes

Figure 15 illustrates the impact of three kinds of Al−5Sr−5Sb modifiers on α(Al) in the AlSi10MnMg alloy. Compared to the SDAS of the unmodified AlSi10MnMg alloy, the SDAS of the modified sample shows improvement. Particularly, the Al−5Sr−5Sb modifier prepared using CDS demonstrates the most effective refinement, with an SDAS of 14.2 μm, which represents a reduction of 22.83% compared to the unmodified alloy. Under normal solidification conditions, the diffusion kinetics indicates that the Sr and Sb distribution coefficients in Al−5Sr−5Sb-modified AlSi10MnMg alloy melt are low. Consequently, these elements accumulate at the solid−liquid interface front, altering the solute distribution and enhancing the subcooling of the alloy. This results in increased α(Al) branching and reduced SDAS size [49,50]. Additionally, the size of the Al_4Sr in the Al−5Sr−5Sb prepared with CDS decreases, facilitating the dissolution of Sr atoms and thereby enhancing the refinement process and reducing the SDAS size of α(Al).

Figure 17 shows the three-dimensional morphology of the eutectic Si phase in the AlSi10MnMg alloys unmodified and after adding the three kinds of Al−5Sr−5Sb modifiers. In the unmodified AlSi10MnMg alloy (Fig. 17(a)), the eutectic Si phase exhibits a lamellar structure with sharp edges, interposed within α(Al). This morphology of the eutectic Si phase is prone to fracture or crack along the edges under stress, leading to compromised mechanical properties of the alloy [51]. In contrast, the eutectic Si phase in

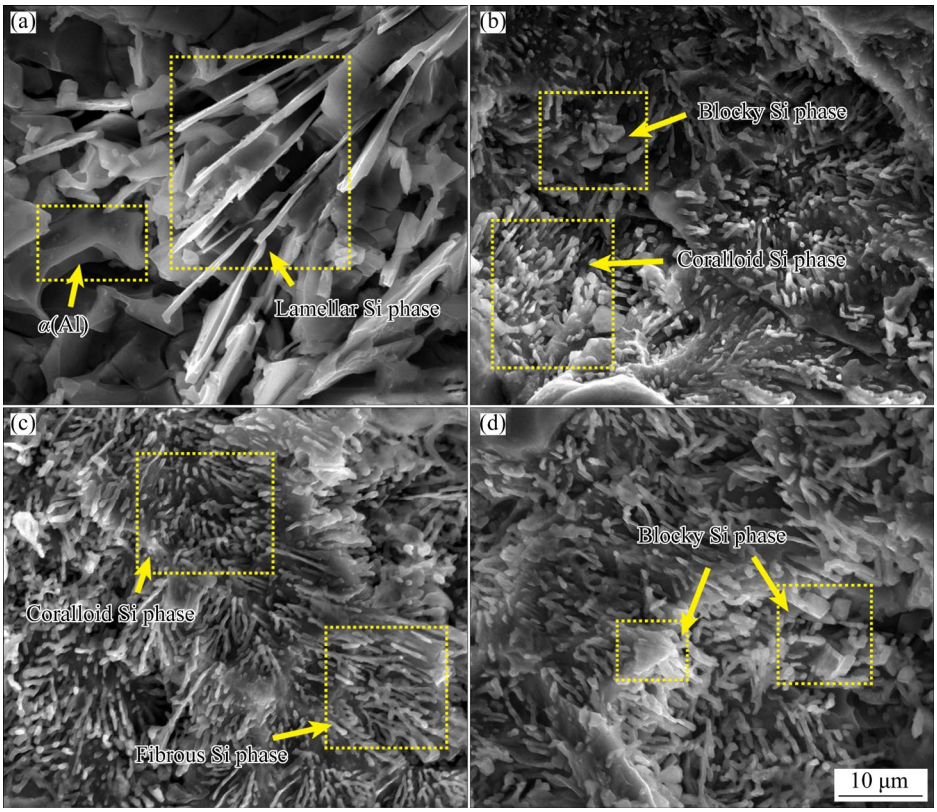

Fig. 17 Morphologies of eutectic Si phase in AlSi10MnMg alloy unmodified (a) and modified by Al−5Sr−5Sb prepared with different processes: (b) PMC; (c) CDS; (d) Rolling

the Al−5Sr−5Sb-modified AlSi10MnMg alloy undergoes significant alteration. The previously sharp lamellar structure is largely replaced by a fine eutectic Si phase, characterized by coral-like and fiber-like features.

Notably, a blocky eutectic Si phase is evident in alloys modified with Al−5Sr−5Sb prepared using PMC (Fig. 17(b)) and rolling (Fig. 17(d)). However, the alloy prepared using CDS exhibits a superior modification, with the eutectic Si phase in the AlSi10MnMg alloy appearing predominantly fine and fiber-like. In summary, the Al−5Sr−5Sb modifier prepared via CDS demonstrates a marginally enhanced modification effect compared to that prepared by PMC and rolling.

Figure 18 shows the EDS surface scanning results for the AlSi10MnMg alloy modified with Al−5Sr−5Sb. These results indicate that most Sr atoms in the modified alloy are adsorbed on the surface of the eutectic Si, thereby decelerating its growth. Regarding antimony, YANEVA et al [52] proposed that AlSb in the melt adsorbs on the eutectic Si surface, inhibiting its growth and consequently refining the eutectic Si. Additionally, AlSb serves as a core for heterogeneous nucleation and is effective when the mismatch degree (δ) is less than 12%, as described by the following equation:

$$\delta = \frac{|\alpha_c - \alpha_N|}{\alpha_N} \tag{7}$$

where α_c represents the atomic spacing of the heterogeneous nucleation masses and α_N denotes the nuclear spacing of the eutectic Si nuclei.

The calculated mismatch (δ) between the eutectic Si phase and AlSb is 13%, indicating that it is challenging for AlSb to act as an effective nucleation particle during cooling. Moreover, adding Sb lowers the eutectic nucleation temperature in the melt, diminishing the eutectic nucleation core [53]. This reduction in the heterogeneous nucleation and melt solidification permits faster growth of eutectic Si at increased subcooling rates, achieving a refining effect.

In Al−5Sr−5Sb modifiers, the modifying effect principally stems from the Al_4Sr and AlSb phases, with efficiency directly linked to the reduced size of these phases. Figure 19 shows a schematic of the modification of eutectic Si by three kinds of Al−5Sr−5Sb modifiers, emphasizing the influence of the size difference between Al_4Sr and AlSb.

The Al−Sr and Al−Si phase diagrams demonstrate that the eutectic transformation of L(Al)+Al_4Sr occurs at 654 °C with a Sr content <20 wt.%. In addition, the eutectic transition temperature of Si in Al is 577 °C, and the eutectic composition is (12.2±0.1) wt.% Si. Thus, the precipitation of Al_4Sr is preceded by the eutectic Si phase. In Al−5Sr−5Sb modifiers, Sr exists in the Al_4Sr phase, with significant modification effects when free Sr dissolves from Al_4Sr. The decomposition of the Al_4Sr phase is expressed as

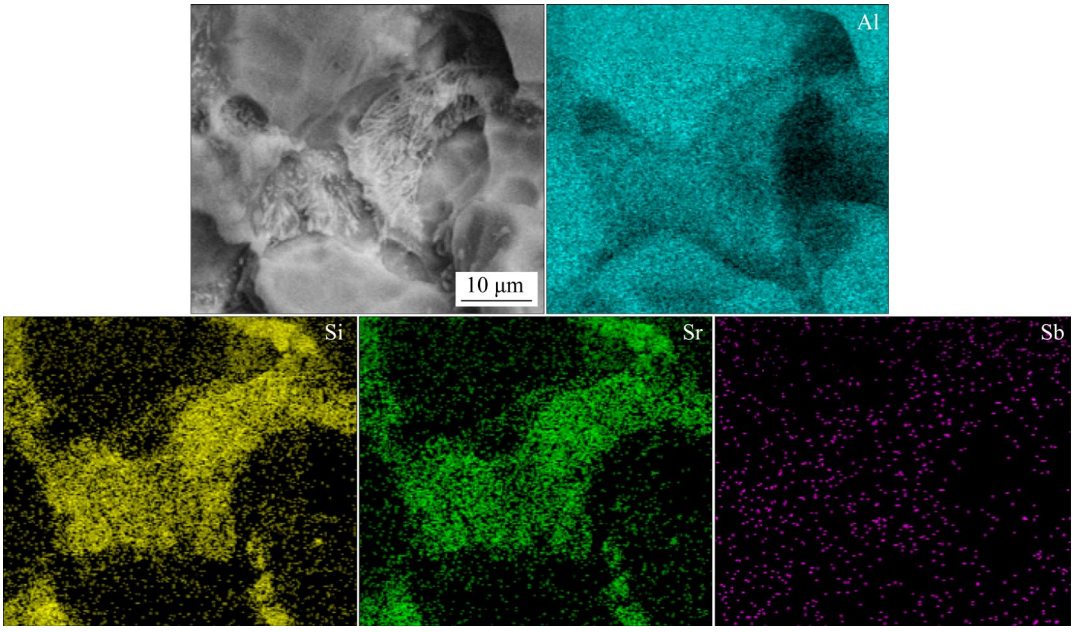

Fig. 18 EDS surface scanning results of AlSi10MnMg alloy modified with Al−5Sr−5Sb

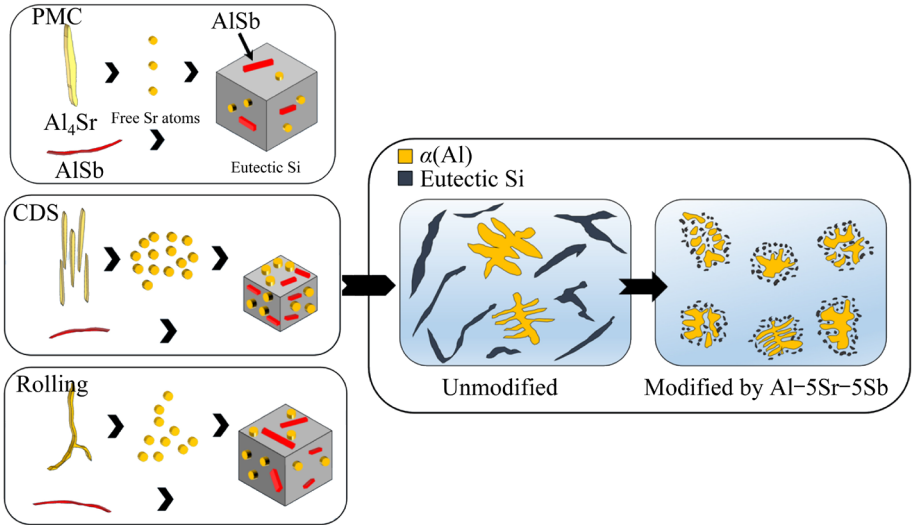

Fig. 19 Schematic diagram of modification of eutectic Si by Al−5Sr−5Sb with different preparation processes

$$Al_4Sr \rightleftharpoons Sr+4Al \tag{8}$$

According to the reaction kinetics at the solid–liquid interface, the dissolution rate is given by [50]

$$v=-\frac{dm}{dt}=kAC^{n'} \tag{9}$$

where v denotes the dissolution rate, m is the mass of the reactants, t is the reaction time, k is the surface reaction rate constant, A is the reactant interface area, C is the reactant concentration, and n' is the reaction order.

During modification with Al−5Sr−5Sb, the constants usually include k and C, implying that the interfacial area directly impacts the reaction rate, v, and time, t. Al_4Sr in Al−5Sr−5Sb prepared via PMC has a large size, small specific surface area, and limited interfacial area (A), leading to slower dissolution of Al_4Sr from free Sr atoms and a prolonged reaction time. Conversely, Al_4Sr prepared by CDS and rolling, with smaller sizes and larger surface areas, facilitates rapid dissociation of Sr atoms from Al_4Sr under identical conditions. Furthermore, the CDS-prepared Al−5Sr−5Sb modifier, which has the lowest melting enthalpy and highest system energy, enhances the diffusion of free Sr more rapidly than PMC and rolling. This rapid enrichment at the Si phase growth front restricts Si phase growth, encouraging branching.

Additionally, Sb in Al forms a stable AlSb phase, adsorbing at the Si phase growth front interface and limiting its lateral growth. The modification size also influences the AlSb effect; larger AlSb phases reduce the involvement in Si phase growth. Consequently, a larger AlSb size indicates less effective inhibition of the Si phase and inferior modification effectiveness [50].

Figure 20 shows the properties of the AlSi10MnMg alloy modified by three kinds of Al−5Sr−5Sb modifiers. The improvements in various properties of the modified AlSi10MnMg alloy are observed. The best preparation methods for the Al−5Sr−5Sb modifiers are CDS, rolling, and PMC, which is consistent with the modification effects observed for the AlSi10MnMg alloys. The thermal conductivity of the AlSi10MnMg alloy modified with Al−5Sr−5Sb prepared by CDS reaches 189.63 W/(m·K), with 24.14% increase compared to 152.77 W/(m·K) for the unmodified alloy. The elongation increases to 10.87%, with 59.15% enhancement, and the tensile strength reaches 254.98 MPa, with 66.9% improvement.

The stress–strain curves reveal that the different preparation processes of Al−5Sr−5Sb have minimal effects on the yield strength of AlSi10MnMg. Under tensile loading, the yield limit is a characteristic of the plastic and elastic strain regime boundary [54]. Given the low stresses involved and the eutectic Si phase in the alloys being significantly refined by the modification, the sources of fracture that diminish the mechanical properties are almost eliminated. Thus, the preparation method of Al−5Sr−5Sb does not appear to have a significant effect on this property.

Figure 21 compares the properties of the AlSi10MnMg alloy prepared in this study with

those of other existing high-thermal-conductivity aluminum alloys, focusing on thermal conductivity, elongation, and tensile strength. The data show the superior thermal conductivity and mechanical properties of the aluminum alloy prepared in this study. The AlSi10MnMg alloy, modified using CDS-prepared Al−5Sr−5Sb, demonstrates a balance between the mechanical properties and thermal conductivity, enhancing various properties of the alloy. Additionally, the AlSi10MnMg and Al−5Sr−5Sb modifiers offer broad market and application potential due to their simple preparation and low equipment requirements.

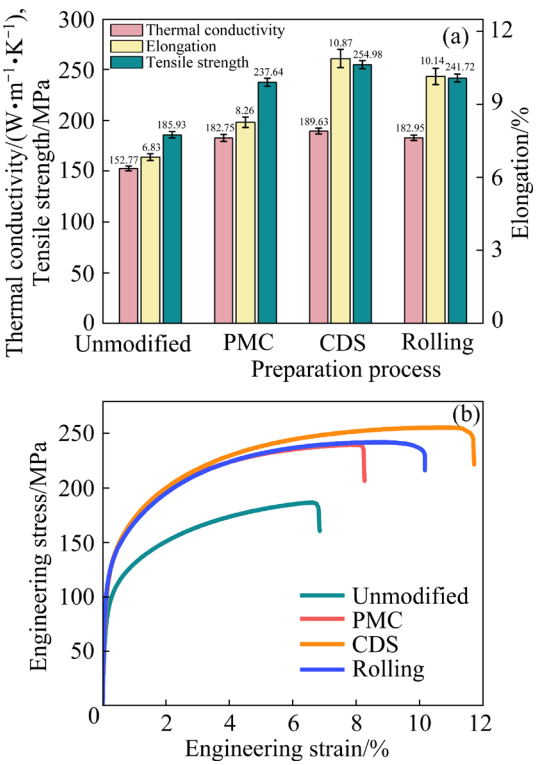

Fig. 20 Properties of AlSi10MnMg alloys modified by Al−5Sr−5Sb with different preparation processes

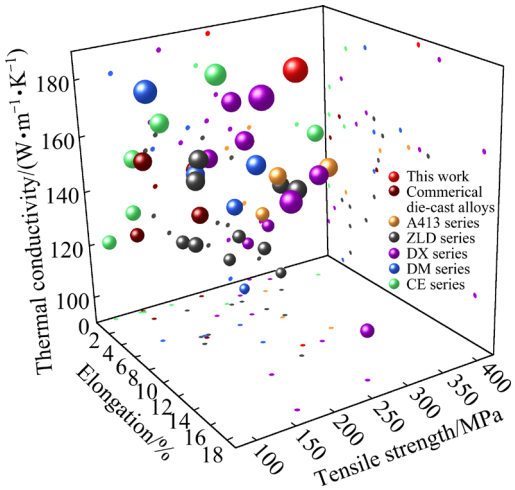

Fig. 21 Properties of alloy in this work compared with those of other existing high thermal conductivity aluminum alloys

The eutectic Si phase in the AlSi10MnMg alloy significantly influences the alloy's properties. According to Griffith's strength theory [55], the overall strength of an alloy is determined by the maximum stress the particles can endure, expressed as follows:

$$\sigma_c = k_c d^{-1/2} \tag{10}$$

where σ_c denotes the maximum stress on the particle, k_c is the fracture roughness of the particle, and d represents the particle diameter. In the AlSi10MnMg, k_c is considered constant, so the eutectic Si size determines σ_c. A smaller eutectic Si size results in a higher maximum stress endurance, thereby enhancing the overall strength of the alloy. Additionally, transforming the thick lamellar eutectic Si in AlSi10MnMg, when modified with Al−5Sr−5Sb, into fine coral-like and fiber-like structures eliminates the microcracks, thus improving the strength.

The thermal conductivity of an alloy is associated with free electron movement. Efficient electron transfer is correlated with better thermal conductivity. The Si phase morphology and size significantly affect electron movement in Al−Si alloys. According to Matthiessen's law [56,57], the resistivity (ρ) of metallic materials is given by

$$\rho = \rho_T + \rho_R \tag{11}$$

where ρ is the total resistivity, ρ_T is the base resistivity, and ρ_R is the resistivity affected by other factors.

ρ_T is related to temperature, while ρ_R is associated with the microstructure of the material and is expressed as

$$\rho_R = \rho_{gb} + \rho_p + \rho_d + \rho_{ss} \tag{12}$$

where ρ_{gb} represents the resistivity influenced by grain boundaries, ρ_p by the second phase of the alloy, ρ_d by electron scattering due to dislocations, and ρ_{ss} by the resistivity effect of the solute atoms. In AlSi10MnMg, the thermal conductivity is mainly impacted by ρ_p, with other factors having less or negligible effects.

In the AlSi10MnMg alloy, the thermal conductivity is primarily influenced by ρ_p, while other factors exert less impact, often negligible. Eutectic Si minimally affects the scattering of free

electrons, leading to an increase in the average free range of electrons and an increase in the thermal conductivity of the alloy.

Figure 22 illustrates the impact of the eutectic Si boundary morphology on the electron scattering in the AlSi10MnMg alloy. In unmodified alloys, thick, needle-shaped, lamellar eutectic Si obstructs electron transport, resulting in poor thermal conductivity. The introduction of the Al−5Sr−5Sb modifier significantly reduces the eutectic Si size, and changes it to fine, coral-like, and fiber-like shape, thereby enhancing the electron transfer efficiency and thermal conductivity [58].

Figure 23 shows the fracture morphologies of the AlSi10MnMg alloy before and after the modification. Figure 23(a) shows the fracture morphology of the unmodified alloy, characterized by quasi-cleavage platforms and a few dimples, which is indicative of a quasi-cleavage fracture mode. The cleavage platform area is small. Figures 23(b−d) reveal the fracture morphologies of the alloy after modification with various kinds of Al−5Sr−5Sb modifier. These images display numerous dimples with small size and uniformly distributed. A comparison indicates that the number and size of dimples in the alloy modified by CDS-prepared Al−5Sr−5Sb are smaller than those by PMC- and rolling-prepared Al−5Sr−5Sb, with the number of dimples following the order of CDS > rolling > PMC.

In conclusion, the principal factor contributing to the improved elongation after modification with Al−5Sr−5Sb is the alteration in the shape and size of the eutectic Si phase. The thick lamellar Si phase transforms into coral-like and fiber-like phases, and the size of the modified Si phase decreases, reducing the likelihood of the lamellar Si phase severing through the Al matrix. Additionally, small and nearly granular Si provides dispersion strengthening to the alloy, thereby enhancing the mechanical properties, particularly the toughness.

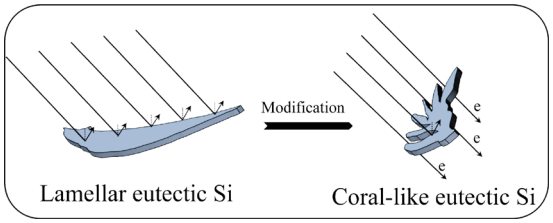

Fig. 22 Effect of eutectic Si phase boundary morphology on electron scattering

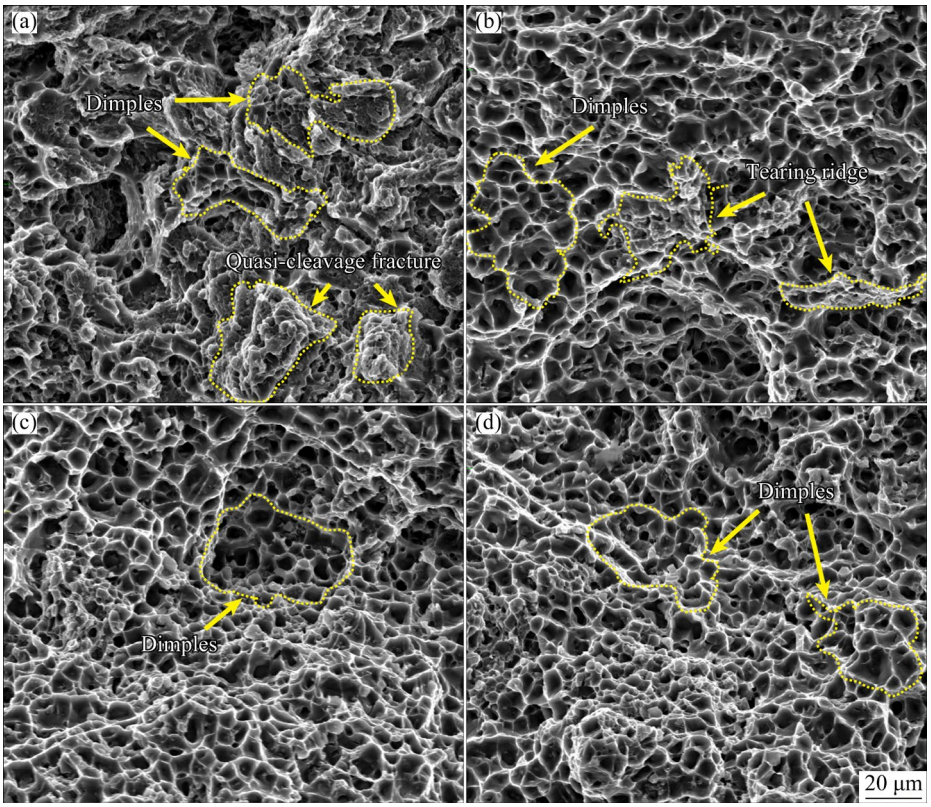

Fig. 23 Fracture morphologies of AlSi10MnMg alloy unmodified (a) and modified with Al−5Sr−5Sb by different preparation processes: (b) PMC; (c) CDS; (d) Rolling

4 Conclusions

(1) CDS and rolling surpass PMC in the preparation of the Al−5Sr−5Sb modifier. The Al_4Sr, AlSb, and Sr_2Sb phases are present in the modifier. Both CDS and rolling refine the microstructure of the modifiers, with CDS being more effective. The Al−5Sr−5Sb prepared via the CDS exhibits the lowest melting enthalpy, ΔH_m=308.9 J/g, as determined by the DSC curve. Consequently, the diffusion of free Sr in Al_4Sr is more robust, and Sb more effectively refines the Si phase.

(2) The crystal structure and elastic modulus of the phases in Al−5Sr−5Sb were computed using first principles, and the Debye temperature of these phases was calculated. The results reveal that Al_4Sr and AlSb possess higher Debye temperatures and bonding strengths. Sr_2Sb demonstrates superior brittleness and deformation resistance; however, its lower Debye temperature negatively impacts the overall thermal conductivity of the modified Al−Si alloy.

(3) Al−5Sr−5Sb effectively refines the α(Al) in the AlSi10MnMg alloy and alters the eutectic Si phase from thick lamellar to coral-like or fiber-like. The CDS-prepared Al−5Sr−5Sb achieves the most effective modification, reducing the SDAS of α(Al) to 14.2 μm, with 22.83% decrease compared to that of the premodified alloy; the blocky eutectic Si is eliminated, enhancing the modification effect.

(4) After modification with Al−5Sr−5Sb, the eutectic Si in the AlSi10MnMg alloy transforms into coral-like and fiber-like shape. The thermal conductivity and mechanical properties of the alloy are improved significantly. The CDS-prepared Al−5Sr−5Sb yields the most notable enhancement, increasing the thermal conductivity of the AlSi10MnMg alloy by 24.14% to 189.63 W/(m·K), enhancing the elongation by 59.15% to 10.87%, and improving the tensile strength by 66.9% to 254.98 MPa.

CRediT authorship contribution statement

Wen-jing LIU: Conceptualization, Methodology, Investigation, Formal analysis, Data curation, Visualization, Writing − Original draft; **Yuan-dong LI:** Conceptualization, Supervision, Writing − Review & editing, Funding acquisition; **Zi-chen WANG:** Investigation, Methodology, Formal analysis; **Xiao-mei LUO:** Investigation, Methodology; **Hong-wei ZHOU:** Investigation, Methodology; **Guang-li BI:** Supervision, Funding acquisition.

Declaration of competing interest

The authors declare that they have no known competing financial interests or personal relationships that could have appeared to influence the work reported in this paper.

Acknowledgments

This research was supported by Gansu Provincial Basic Research Program−Natural Science Fund, China (No. 22JR5RA251) and Science Fund for Distinguished Young Scholars of Gansu Province, China (No. 23JRRA785).

References

[1] ZHOU Wei, WANG Ri-chu, PENG Chao-qun, CAI Zhi-yong. Microstructure and properties of Al−Si functionally graded materials for electronic packaging [J]. Transactions of Nonferrous Metals Society of China, 2023, 33: 3583−3596.

[2] YUAN Zi-hao, GUO Zhi-peng, XIONG Shou-mei. Microstructure evolution of modified die-cast AlSi10MnMg alloy during solution treatment and its effect on mechanical properties [J]. Transactions of Nonferrous Metals Society of China, 2019, 29: 919−930.

[3] DU Shang-zhe, ZHANG Cheng-cheng, FENG Kai, LI Zhu-guo, ZHU Jie, FENG Yu-lei, PAN Xin, JIA Jun. A comparative investigation on corrosion behaviors of high pressure die-cast Al−Si alloys in 3.5% NaCl solution [J]. International Journal of Electrochemical Science, 2022, 17: 22125.

[4] ZHANG Wen, XU Jun. Advanced lightweight materials for automobiles: A review [J]. Materials & Design, 2022, 221: 110994.

[5] JEON J H, BAE D H. Effect of cooling rate on the thermal and electrical conductivities of an A356 sand cast alloy [J]. Journal of Alloys and Compounds, 2019, 808: 151756.

[6] SHIN J, KO S, KIM K. Development and characterization of low-silicon cast aluminum alloys for thermal dissipation [J]. Journal of Alloys and Compounds, 2015, 644: 673−686.

[7] LI Yang, HU Bin, LIU Bin, NIE An-min, GU Qin-fen, WANG Jian-feng, LI Qian. Insight into Si poisoning on grain refinement of Al−Si/Al−5Ti−B system [J]. Acta Materialia, 2020, 187: 51−65.

[8] DAHLE A K, NOGITA K, MCDONALD S D, DINNIS C, LU L. Eutectic modification and microstructure development in Al−Si alloys [J]. Materials Science and Engineering A, 2005, 413/414: 243−248.

[9] HEGDE S, PRABHU K N. Modification of eutectic silicon in Al−Si alloys [J]. Journal of Materials Science, 2008, 43: 3009−3027.

[10] ZHOU Yu-li, ZHANG Xun, ZHONG Gu, ZHANG Jun-chao, YANG Yang, KANG Du, LI Hu-tian, JIE Wan-qi, SCHUMACHER P, LI Jie-hua. Elucidating thermal conductivity mechanism of Al−9Si based alloys with trace transition elements (Mn, Cr, V) [J]. Journal of Alloys and Compounds, 2022, 907: 164446.

[11] GURSOY O, TIMELLI G. The role of bismuth as trace

element on the solidification path and microstructure of Na-modified AlSi7Mg alloys [J]. Advanced Engineering Materials, 2023, 25: 2201377.

[12] LI J H, ALBU M, HOFER F, SCHUMACHER P. Solute adsorption and entrapment during eutectic Si growth in Al−Si-based alloys [J]. Acta Materialia, 2015, 83: 187−202.

[13] SIGWORTH G, CAMPBELL J, JORSTAD J. The modification of Al−Si casting alloys: Important practical and theoretical aspects [J]. International Journal of Metalcasting, 2009, 3: 65−78.

[14] LUO Qun, LI Xing-rui, LI Qian, YUAN Ling-yang, PENG Li-ming, PAN Fu-sheng, DING Wen-jiang. Achieving grain refinement of α-Al and Si modification simultaneously by La−B−Sr addition in Al–10Si alloys [J]. Journal of Materials Science & Technology, 2023, 135: 97−110.

[15] YI Wang, LIU Guang-chen, LU Zhao, GAO Jian-bao, ZHANG Li-jun. Efficient alloy design of Sr-modified A356 alloys driven by computational thermodynamics and machine learning [J]. Journal of Materials Science & Technology, 2022, 112: 277−290.

[16] GAN Jun-qi, HUANG Yu-jian, WEN Cheng, DU Jun. Effect of Sr modification on microstructure and thermal conductivity of hypoeutectic Al−Si alloys [J]. Transactions of Nonferrous Metals Society of China, 2020, 30: 2879−2890.

[17] GUO Jin, GUAN Zhi-ping, YAN Rui-fang, MA Pin-kui, WANG Ming-hui, ZHAO Po, WANG Jin-guo. Effect of modification with different contents of Sb and Sr on the thermal conductivity of hypoeutectic Al−Si alloy [J]. Metals, 2020, 10: 1637.

[18] TANG Peng, LIU Qian-nan, YU Feng-yang, MO Fan, QIN Lu-man. Effect and its mechanism of fixed-ratio and incremented 3Be−Sb complex modifier on microstructures and properties of hypereutectic Al−Si−Mg alloy [J]. Journal of Alloys and Compounds, 2023, 931: 167478.

[19] KARABAY S. Modification of AA-6201 alloy for manufacturing of high conductivity and extra high conductivity wires with property of high tensile stress after artificial aging heat treatment for all-aluminium alloy conductors [J]. Materials & Design, 2006, 27: 821−832.

[20] ZHANG Ming-jie, LI Jin-li, LIANG Jia-xiao. Preparation of Al−Sc alloys by molten salt electrolysis [J]. Journal of Northeastern University, 2003, 24: 358−360. (in Chinese)

[21] LIAO Cheng-wei, CHEN Jian-chun, LI Yang, TU Rui, PAN Chun-xu. Morphologies of Al4Sr intermetallic phase and its modification property upon A356 alloys [J]. Journal of Materials Science & Technology, 2012, 28: 524−530.

[22] ZHOU Hong-wei, LI Yuan-dong, MA Ying, ZHANG Xin-long, LIU Xing-hai. Microstructure and solidification behavior of Al−18%Si hypereutectic alloy prepared by controlled diffusion solidification [J]. The Chinese Journal of Nonferrous Metals, 2014, 24: 1761−1770. (in Chinese)

[23] APELIAN D, MAKHLOUF M M, SAHA D. CDS method for casting aluminum-based wrought alloy compositions: Theoretical framework [J]. Materials Science Forum, 2006, 519/520/521: 1771−1776.

[24] KHALAF A A, SHANKAR S. Favorable environment for a nondendritic morphology in controlled diffusion solidification [J]. Metallurgical and Materials Transactions. A: Physical Metallurgy and Materials Science, 2011, 42: 2456−2465.

[25] GUO Yu, WANG Ye, JIANG Bo, CHEN Hong-tao, XU Hong-yu, HU Mao-liang, JI Ze-sheng. Microstructure evolution, thermal conductivity and mechanical properties of hot-rolling Al−Si−Fe−Mg alloy under different reductions [J]. Modern Physics Letters B, 2022, 36: 2150533.

[26] FARAHANY S, OURDJINI A, IDRIS M H. The usage of computer-aided cooling curve thermal analysis to optimise eutectic refiner and modifier in Al−Si alloys [J]. Journal of Thermal Analysis and Calorimetry, 2012, 109: 105−111.

[27] WANG Jia-jia, LU Zi-jie, ZHANG Kai-xiao, YING Guo-bing, LI Bao-song, CHEN Jian-qing, SONG Dan, JIANG Jing-hua, MA Ai-bin. DFT study on termination stabilities of Mg17Al12 (110) surface [J]. Transactions of Nonferrous Metals Society of China, 2023, 33: 755−764.

[28] KRESSE G, FURTHMÜLLER J. Efficiency of ab-initio total energy calculations for metals and semiconductors using a plane-wave basis set [J]. Computational Materials Science, 1996, 6: 15−50.

[29] XIAO Yao, LAN Xin-yue, LU Qiang, DU Yong, LI Kai. In-situ evidence for rotation of Si particles with respect to grains in tensile-deformed Al−Si alloys [J]. Transactions of Nonferrous Metals Society of China, 2023, 33: 1655−1664.

[30] PFROMMER B G, CÔTÉ M, LOUIE S G, COHEN M L. Relaxation of crystals with the Quasi-Newton method [J]. Journal of Computational Physics, 1997, 131: 233−240.

[31] SHAM L J, KOHN W. Self-consistent equations including exchange and correlation effects [J]. Physical Review, 1965, 140: 1133−1138.

[32] PERDEW J P, BURKE K, ERNZERHOF M. Generalized gradient approximation made simple [J]. Physical Review Letters, 1996, 77: 3865−3868.

[33] KHALAF A A. Mechanism of controlled diffusion solidification: Mixing, nucleation and growth [J]. Acta Materialia, 2016, 103: 301−310.

[34] KHALAF A A, ASHTARI P, SHANKAR S. Formation of nondendritic primary aluminum phase in hypoeutectic alloys in controlled diffusion solidification (CDS): A hypothesis [J]. Metallurgical and Materials Transactions B: Process Metallurgy and Materials Processing Science, 2009, 40: 843−849.

[35] WANG Yan-bo, LIAO Xiao-zhou, ZHU Yun-tian. Grain refinement and growth induced by severe plastic deformation [J]. International Journal of Materials Research, 2009, 100: 1632−1637.

[36] CHANG Liang, DING Yu-ming, GUO Bin-xu, DING Jian, XIA Xing-chuan, TANG Ying, LI Chong, SUN Xiao-mian, GUO Jun-jie, SONG Kai-hong, WANG Li-sheng, ZHOU Kai-peng, CHEN Xue-guang, LIU Yong-chang. Modification mechanism and tensile property of Al−9Si−0.4Mg−0.1Cu alloy [J]. Materials Characterization, 2022, 184: 111693.

[37] ZHANG Zhen, HU Jia-min, TENG Jie, CHEN Jian-chun, ZHAO Guo-dong, JIANG Fu-lin, FU Ding-fa, ZHANG Hui. Hot compression and industrial extrusion characteristics of an as-cast Al−10Sr master alloy [J]. Journal of Manufacturing Processes, 2021, 61: 481−491.

[38] FATAHALLA N, HAFIZ M, ABDULKHALEK M. Effect of microstructure on the mechanical properties and fracture of commercial hypoeutectic Al−Si alloy modified with Na, Sb and Sr [J]. Journal of Materials Science, 1999, 34: 3555−3564.

[39] ZHANG Z H, BIAN X F, WANG Y. Microstructural characterisation of nanoscale eutectics in melt spun Al−10Sr alloy [J]. Materials Science and Technology, 2002, 18:

1092−1096.
[40] ZHANG Yang-yang. The influence of Al-10Sr modifier and cooling rate in different states on the microstructure and properties of ZL114A alloy [D]. Jilin University, 2016. (in Chinese)
[41] IVANOV M I, ROMANOVA L O, SHEVCHENKO M O, SUDAVTSOVA V S, KUDIN V G. Mixing enthalpies of Sr−Sb melts [J]. Powder Metallurgy and Metal Ceramics, 2020, 58: 725−729.
[42] ALI K, ARYA A, GHOSH P S, DEY G K. A first principles study of cohesive, elastic and electronic properties of binary Fe−Zr intermetallics [J]. Computational Materials Science, 2016, 112: 52−66.
[43] ANDERSON O L. A simplified method for calculating the Debye temperature from elastic constants [J]. Journal of Physics and Chemistry of Solids, 1963, 24: 909−917.
[44] PUGH S F. XCII. Relations between the elastic moduli and the plastic properties of polycrystalline pure metals [J]. The London, Edinburgh, and Dublin Philosophical Magazine and Journal of Science, 2009, 45: 823−843.
[45] MOHRI T, CHEN Y, KOHYAMA M, OGATA S, SAENGDEEJING A, BHATTACHARYA S K, WAKEDA M, SHINZATO S, KIMIZUKA H. Mechanical properties of Fe-rich Si alloy from Hamiltonian [J]. npj Computational Materials, 2017, 3: 10.
[46] SHANG Shun-Li, WANG Yi, KIM D E, LIU Zi-Kui. First-principles thermodynamics from phonon and Debye model: Application to Ni and Ni_3Al [J]. Computational Materials Science, 2010, 47: 1040−1048.
[47] FAN Qiang, LIU Chun-hai, YANG Jian-hui. The physical properties of Sc2PbC: A first-principles calculations [J]. Results in Physics. 2023, 53: 107013.
[48] RAMESHKUMAR S, JAIGANESH G, JAYALAKSHMI V. Structural, phonon, elastic, thermodynamic and electronic properties of Mg−X (X = La, Nd, Sm) intermetallics: The first principles study [J]. Journal of Magnesium and Alloys, 2019, 7: 166−185.
[49] CESCHINI L, MORRI A, TOSCHI S, JOHANSSON S, SEIFEDDINE S. Microstructural and mechanical properties characterization of heat treated and overaged cast A354 alloy with various SDAS at room and elevated temperature [J]. Materials Science and Engineering A, 2015, 648: 340−349.
[50] VASUDEVAN G, ANBUKKARASI R, SANIL H, RAVI M. Combined effect of Sr-addition and pressure induced solidification on eutectic-Si morphology and mechanical properties of squeeze cast Al-Si binary alloy [J]. Materials Today Communications, 2023, 34: 105104.
[51] DING Wan-wu, GOU Lu-min, HU Li-wen, ZHANG Hai-xia, ZHAO Wen-jun, MA Jin-yuan, QIAO Ji-sen, LI Xiao-chun. Modification of eutectic Si in hypoeutectic Al-Si alloy with novel Al−3Ti−4.35La master alloy [J]. Journal of Alloys and Compounds, 2022, 929: 167350.
[52] YANEVA S, STOJANOVA L, STOICHEV N, KAMENOVA Z. On the mechanism of Al−Si alloy structure modification by metal antimony [J]. Crystal Research and Technology, 1988, 23: 475−480.
[53] YEREMENKO V N, NATANZON Y V, DYBKOV V I. The effect of dissolution on the growth of the Fe_2Al_5 interlayer in the solid iron-liquid aluminium system [J]. Journal of Materials Science, 1981, 16: 1748−1756.
[54] OBARA T J, MINEI R O, KAKITANI R, SPINELLI J E, GARCIA A, CHEUNG N. Solidification microstructure and mechanical properties of an Al−11wt.%Si alloy modified with Nb and Sb [J]. Journal of Physics and Chemistry of Solids, 2023, 181: 111521.
[55] GRIFFITH A A, TAYLOR G I. VI. The phenomena of rupture and flow in solids [J]. Philosophical Transactions of the Royal Society of London, 1997, 221: 163−198.
[56] TIAN L, ANDERSON I, RIEDEMANN T, RUSSELL A. Modeling the electrical resistivity of deformation processed metal–metal composites [J]. Acta Materialia, 2014, 77: 151−161.
[57] MACDONALD D K C, SARGINSON K, SIMON F E. Size effect variation of the electrical conductivity of metals [J]. Philosophical Transactions of the Royal Society of London: A, 1950, 203: 223−240.
[58] WANG Guan-yi, GUAN Zhi-ping, WANG Jin-guo, REN Ming-wen, YAN Rui-fang, SONG Jia-wang. Effect of cooling rate and modification by strontium on the thermal conductivity of Al−8Si alloy [J]. Metals, 2021, 11: 1334.

不同工艺制备的 Al−5Sr−5Sb 变质剂对 AlSi10MnMg 合金显微组织、热导率及力学性能的影响

刘文憬[1]，李元东[1,2]，王梓臣[1]，罗晓梅[1]，周宏伟[1,2]，毕广利[1,2]

1. 兰州理工大学 省部共建有色金属先进加工与再利用国家重点实验室，兰州 730050；
2. 兰州理工大学 有色金属合金及加工教育部重点实验室，兰州 730050

摘 要：采用金属型铸造(PMC)、受控扩散凝固(CDS)和轧制制备了 3 种 Al−5Sr−5Sb 变质剂。通过 DSC 曲线评估熔化焓和第一原理计算，研究制备方法对 Al−5Sr−5Sb 的影响。将 3 种 Al−5Sr−5Sb 添加至 AlSi10MnMg 合金中，以研究变质效果和机理。结果表明，CDS 制备的 Al−5Sr−5Sb 是 AlSi10MnMg 合金中最有效的改性剂，可将共晶 Si 相从片状结构转变为细小的珊瑚状或纤维状结构。与未变质的合金相比，经 CDS 制备的 Al−5Sr−5Sb 变质后，AlSi10MnMg 合金的热导率提高了 24.14%，达到 189.63 W/(m·K)；伸长率提高了 59.15%，达到 10.87%；抗拉强度提高了 66.9%，达到 254.98 MPa。

关键词：受控扩散凝固；变质；AlSi10MnMg；第一性原理；热导率；力学性能

(Edited by Bing YANG)